

Speckle2Speckle: Unsupervised Learning of Ultrasound Speckle Filtering Without Clean Data

Rüdiger Göbl

Computer Aided Medical Procedures, Technical University Munich, Munich, Germany
OneProjects Design Innovation GmbH, Munich, Germany

r.goebl@tum.de

Christoph Hennemersperger

Computer Aided Medical Procedures, Technical University Munich, Munich, Germany
OneProjects Design Innovation GmbH, Munich, Germany

christoph.hennemersperger@tum.de

Nassir Navab

Computer Aided Medical Procedures, Technical University Munich, Munich, Germany

nassir.navab@tum.de

Abstract

In ultrasound imaging the appearance of homogeneous regions of tissue is subject to speckle, which for certain applications can make the detection of tissue irregularities difficult. To cope with this, it is common practice to apply speckle reduction filters to the images. Most conventional filtering techniques are fairly hand-crafted and often need to be finely tuned to the present hardware, imaging scheme and application. Learning based techniques on the other hand suffer from the need for a target image for training (in case of fully supervised techniques) or require narrow, complex physics-based models of the speckle appearance that might not apply in all cases. With this work we propose a deep-learning based method for speckle removal without these limitations. To enable this, we make use of realistic ultrasound simulation techniques that allow for instantiation of several independent speckle realizations that represent the exact same tissue, thus allowing for the application of image reconstruction techniques that work with pairs of differently corrupted data. Compared to two other state-of-the-art approaches (non-local means and the Optimized Bayesian non-local means filter) our method performs favorably in qualitative comparisons and quantitative evaluation, despite being trained on simulations alone, and is several orders of magnitude faster. Our code is available at <https://github.com/goeblr/Speckle2Speckle>.

Keywords: CNN, Deep Learning, Speckle filtering, Ultrasound, Unsupervised

1. Introduction

Ultrasound imaging is a valuable tool to support non-invasive diagnosis and for use during interventions, as it is portable, affordable and does not subject the patient or staff to ionizing radiation. It is not, however, without problems. One of the major differences between CT and MRI on the one hand and ultrasound on the other hand is the presence of speckle, a grainy, noiselike image degradation that even affects tissue regions that are homogeneous in their microstructure such as liver or thyroid tissue (*e.g.* see Figure 1a). This speckle can make interpretation of the images difficult—especially for users with limited experience working with ultrasound. Consequently, most—if not all—ultrasound systems apply speckle reduction techniques after image formation, where the amount of "graininess" that is retained usually can be controlled by the user through a linear combination or

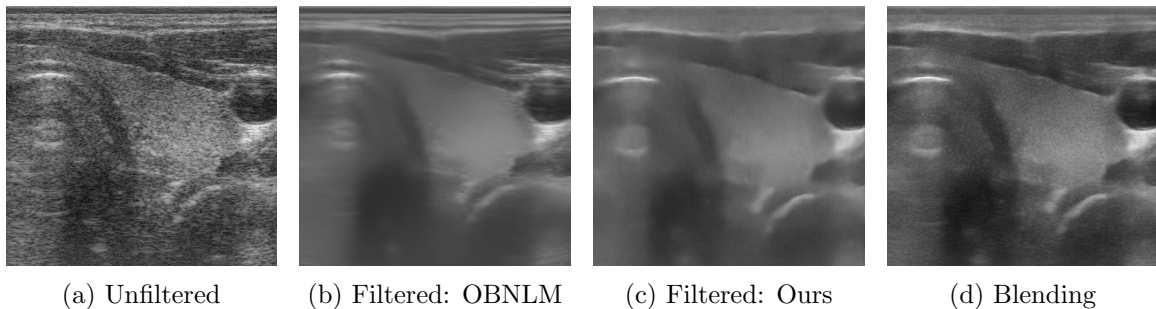


Figure 1: Comparison of image appearance of a thyroid. Unfiltered (a), despeckling with a state-of-the-art method (OBNLM) (b), despeckling with our method (c) and a linear combination of (a) and (c) in (d).

blending of filtered and unfiltered data, depending on the clinical task and user preference. Figure 1 shows a thyroid image before and after filtering with our method compared to a state-of-the-art method and outlines a way to preserve a controlled amount of speckle.

The speckle patterns that emerge in ultrasound images are directly influenced by the location of sub-resolution scatterers in the medium. Being (spaced) sub-resolution, the reflections caused by the individual scatterers cannot be separated by the ultrasound imaging system. The result is interference between the echoes of different amplitude and phase, leading to an apparent echogenicity that changes depending on the spatial configuration of the scatterers within each resolution cell and the orientation of transmitting and receiving elements. In addition to speckle, there is also electronic noise that degrades ultrasound images, which is not the focus of this work. Speckle, while sometimes referred to as noise, is a deterministic phenomenon. In fact, if it were possible to place an ultrasound transducer at the exact same location when repeating a scan, the resulting speckle pattern would be exactly the same.

2. Related Works and Contribution

Conventional despeckling approaches such as speckle-reducing anisotropic diffusion (SRAD) (Yu and Acton, 2002) and the Optimized Bayesian non-local means filter (OBNLM) (Coupé et al., 2009)—itself building upon non-local means (NLM) (Buades et al., 2005)—have been studied extensively. We refer the interested reader to the review from Mohd Sagheer and George (2020). Especially the latter method OBNLM exhibits excellent despeckling performance, but requires application-specific tuning and significant processing time.

Cammarasana et al. (2021) alleviate both these concerns by using a regression CNN that is trained against images despeckled with a tuned, computationally expensive conventional method, thereby allowing the CNN to replicate its results while lowering the execution time.

In other areas different to ultrasound imaging, there exists a body of work on the task of image denoising without requiring perfectly matched pairs of corrupted and clean data. In Noise2Noise (Lehtinen et al., 2018), a CNN learns to restore images from a number of different corruptions, by using a corrupted image as input and a second image of the same "scene" with a different realization of the corruption as training target. The authors show

that this can reach the performance of methods training against clean images. Noise2Void (Krull et al., 2019) takes this even further by requiring only unpaired corrupted images, it requires however, strong assumptions on the corruption, namely zero-mean and per-pixel independent noise.

Given the difficulties of acquiring clean images in many medical imaging modalities, these general approaches have been further specialized. In optical coherence imaging, a few well-chosen modifications to the acquisition setup can allow for the acquisition of two independent speckle instances with otherwise unchanged scanning setup (Yin et al., 2020), effectively allowing for direct use of Noise2Noise. However, this method cannot be directly applied to ultrasound imaging, as these modifications are not possible in ultrasound scanning setups.

In this work, we build on the concept of exploiting two independent *corrupted* observations with the same scanning setup and geometry, and transfer this to a generalizable method for ultrasound imaging. In this way, we present a technique for learning a CNN-based ultrasound despeckle filter only from images containing speckle. To do so, we apply the concept of Noise2Noise (Lehtinen et al., 2018), combined with a scheme for ultrasound simulation for data generation, and modifications to the training loss to enhance the image appearance in a method we call Speckle2Speckle. By simulating different observations of the same general anatomical geometry but with different scatterer locations, we create images with uncorrelated speckle patterns. In our qualitative comparison and quantitative evaluation with state-of-the-art approaches, we show that the method can remove speckle from real ultrasound data efficiently while not relying on manual data annotation or acquisitions, while the application of the filter is several orders of magnitude faster.

3. Method

In this section we first summarize the original formulation of Noise2Noise, followed by a description how we create simulated ultrasound images to be used with a denoising approach like this, and the modifications that were required to account for the peculiarities of ultrasound. Figure 2 shows a comparison between the concepts for conventional (clean-target) (Cammarasana et al., 2021), Noise2Noise and Speckle2Speckle filter learning.

3.1 Noise2Noise

Noise2Noise (Lehtinen et al., 2018) is a deep-learning based technique for general image restoration that does not require clean, uncorrupted data for training. In a conventional restoration approach, one would use corrupted images as input and clean images of the same scene as the training target. In their work however, Lehtinen *et al.* derive, from a statistical perspective, that a network trained with infinite samples can learn to estimate the expectation of the target samples. This allows the input images as well as the target images to be corrupted with noise, like image noise observed with digital image sensors. The authors show that the networks trained in this manner perform on-par with networks trained against clean data.

These relaxed requirements on the training targets allow for the application of this technique to situations where the acquisition of clean targets is either costly or impossible all-together. In their work, Noise2Noise using a modified U-Net (following Ronneberger

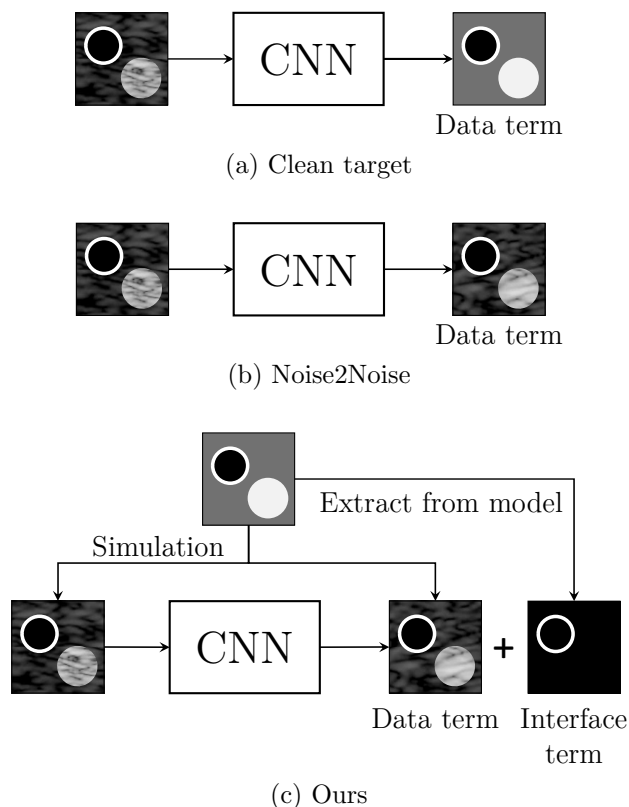


Figure 2: Overview of training a model with corrupted data input to clean data output (a), Noise2Noise training with both corrupted data inputs and outputs of different realizations (b), and Speckle2Speckle training with corrupted realizations of ultrasound data simulated from the same tissue model (c).

et al. (2015), see Figure 3) is applied to a number of different image corruption scenarios ranging from photographs subjected to Gaussian-, Poisson- and Bernoulli-noise or text-overlays, Monte-Carlo rendered images, and even MRI acquisitions within the randomly sampled k-space.

3.2 Speckle2Speckle: Data

Ultrasound imaging is a perfect example for a situation where a noise-free target image is difficult to obtain: since diffuse scattering is present for any ultrasound acquisition, speckle patterns remain visible at any time for acquired echo data. Thus, one can argue that in ultrasound imaging, there is no image without speckle. The strong correlation between the location and scattering behaviour of the tissue inhomogeneities causing the echos and the locations of extrema in the observed reflections (*i.e.*, the speckle pattern), however, makes the acquisition of multiple images with independent corruption (of the desired echogenicity measurement) difficult for real acquisitions.

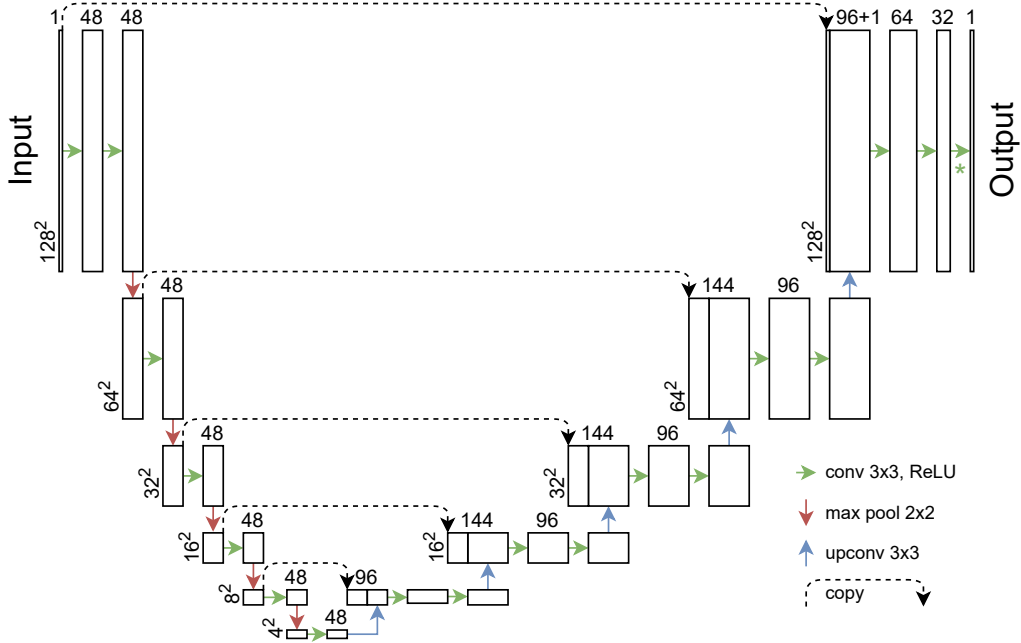


Figure 3: Network architecture of Noise2Noise and Speckle2Speckle. Numbers left of each box show the sizes of the feature maps, exemplified with a 128 by 128 pixel input. The number of channels per feature map is given by the numbers above the boxes. Different arrows represent different operations. The rightmost convolution (marked with $*$) has linear activation.

However, we can instead turn to realistic ultrasound simulations, where we can exploit the specific control over individual scatterers to generate an arbitrary amount of corrupted datasets for a given setup. The training data for Speckle2Speckle is generated with the simulation software Field II (Jensen and Svendsen, 1992; Jensen, 1996). Images are generated in pairs, using independent in-silico scatterer phantom datasets (collections of scatterers with associated scattering strengths). These in-silico scatterer phantom datasets are derived from the same geometric phantom, which is a collection of 3D shapes each of which with a number of parameters describing their appearance in ultrasound imaging and scatterer parameters:

- scatterer density
- scatterer amplitude distribution
- presence or absence of an interface
- interface scatterer density
- interface scatterer amplitude distribution

Based on these properties, this approach allows for the generation of scatterer phantom datasets with independent scatterer locations and thus ideally suited for approaches such

as Noise2Noise. Scatterer locations can be generated randomly, but since the "macro-scale" geometry (e.g. areas of higher scattering) is the same, the ultrasound images created from the different scatterer phantoms look structurally identical and even the speckle distributions are identical. The main difference, however, is that the speckle pattern "instance" is different, for which an example is shown in Figure 4a and Figure 4b.

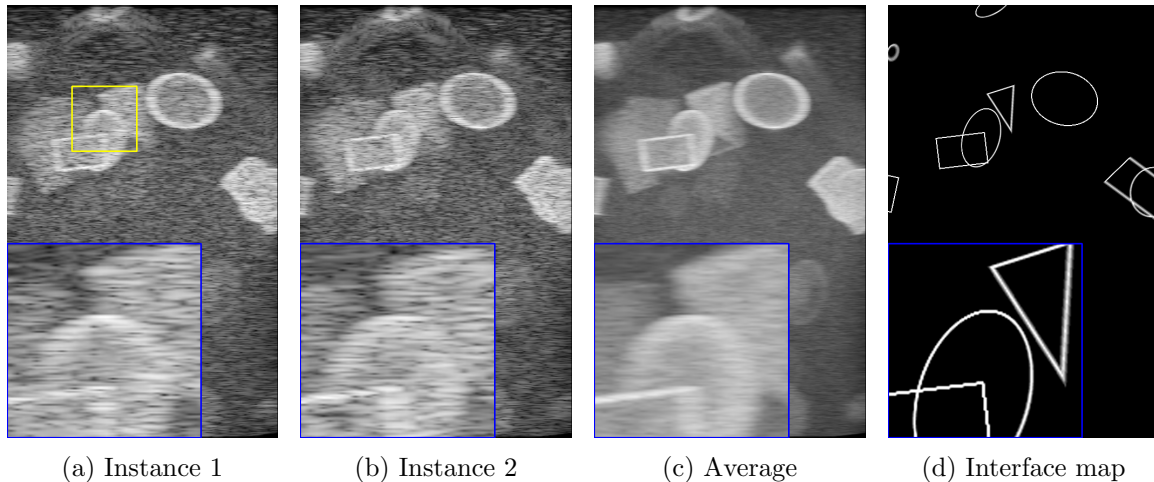


Figure 4: Comparison of the different image types created through simulation: Ultrasound images of two different scatterer instances from the same phantom geometry (a) and (b), average of nine ultrasound images from the same geometry (c), interface map derived from the phantom geometry (d).

While the training is performed with pairs of scatterer instances, we use a different target for the testing and validation. In order to facilitate the evaluation of speckle removal in the absence of noise-free images, we compare the output of our method with an image that is composed by averaging multiple ultrasound images of the same phantom geometry but different scatterer instances. For the training and validation sets, we generated 10 instances per phantom, one of which is used (randomly) as input, the other nine are averaged. Figure 4c shows the average of nine images corresponding to the same geometry as in Figure 4a and Figure 4b.

In addition to the ultrasound images, we also derive an interface map directly from the geometric phantom. Being of the same size and spatial origin as the simulated ultrasound images, it contains whether an interface of a shape was present at each location. Figure 4d shows the interface map associated with the geometry used for the simulations of the ultrasound images in Figure 4. This is later utilized to adapt the training loss to the challenges of ultrasound imaging in order to achieve enhancements of prominent interfaces in the output.

Following this general scheme, a dataset was generated with a training set consisting of 1000 image pairs while the validation and test sets each contain 100 phantom geometries with 10 speckle instances per phantom geometry, resulting in 4000 simulated images in total. Fundamentally, the size of the dataset was limited by the simulation time, where each image required roughly between one and two days on a single CPU core to simulate (depending

Region	Parameter	Value
Background	probability anechoic	0.4
	scatterer density	$0.333 \times 10^{10} \text{ m}^{-3}$
	scatterer amplitude	normal distributed $\mathcal{N}(0, \sigma_{\text{bg}}^2)$; σ_{bg} drawn per phantom from $\mathcal{N}(1, 0.5^2)$
Inclusion	random objects	spheroids & cuboids, uniformly distributed
	number per phantom	100
	extents	drawn per axis uniformly from $[1, 5]$ mm
	probability anechoic	0.4
	scatterer density	$0.333 \times 10^{10} \text{ m}^{-3}$
	scatterer amplitude	normal distributed $\mathcal{N}(0, \sigma_{\text{inc}}^2)$; σ_{inc} drawn per inclusion from $\mathcal{N}(4, 2^2)$
Inclusion Interface	probability interface	0.5
	scatterer density	$5 \times 10^6 \text{ m}^{-2}$
	scatterer amplitude	constant per inclusion, drawn per inclusion from $\mathcal{N}(14, 2^2)$

Table 1: Simulated phantom parameters and values

on the concrete number of scatterers and the CPU performance), although parallelization between images was trivial.

In order to limit the simulation run-time, the scatterer densities values were determined as high as required such that further increase did not cause a change in the speckle patterns. The probabilities of geometries being anechoic and the scatterer amplitude distributions were determined arbitrarily to ensure visibility of the different regions. The specific parametrization is listed in Table 1.

The simulated imaging protocol used focused imaging and it followed the same restrictions as an actual focused scan using a CPLA12875 probe with a cQuest Cicada (both Cephasonics, CA, USA) would be subject to. Table 2 contains the detailed acquisition parameters.

The output of the simulations was ultrasound radio-frequency channel data, which was subsequently processed to ultrasound images using SUPRA (Göbl et al., 2018) with parameters as in Table 3. After beamforming, the resulting images were converted to PNGs and interface indicator maps for inclusions with an interface were created by examining the geometry at every pixel location for the presence of an interface.

3.3 Speckle2Speckle: Learning

The network architecture employed in Speckle2Speckle follows Noise2Noise (see subsection 3.1).

The training loss, however, was adjusted for the peculiarities of ultrasound imaging. While the original Noise2Noise approach used different loss data terms depending on the noise, we extended the data term L_2 with a term to enhance the appearance of interfaces in the images, as interfaces retain key information for interpreting ultrasound imaging data.

Parameter	Value
transducer	CPLA12875
number elements	128
element pitch	0.30 mm
elevation focus	None
transmit frequency	7 MHz
transmit pulse	bipolar
imaging depth	60 mm
focus depth	30 mm
steering	0°
number scanlines	128
TX aperture size	32
RX aperture size	64

Table 2: Simulated acquisition parameters and values

Parameter	Value
beamforming	DAS with hamming window
dynamic range	70 dB
image resolution	0.075 mm
image width	37.6 mm $\hat{=}$ 502 pixels
image height	60.0 mm $\hat{=}$ 801 pixels

Table 3: Image reconstruction parameters and values

The interface term is based on the known locations of interfaces given by the interface indicator map I_i . We chose $I_{iG} = g_i * I_i$ as spatial weight for the interface loss, where g_i is a 2D Gaussian with standard deviation σ_i . This serves to i) extend the range of the interface effects from the potentially sharp peaks in the interface map, as well as ii) achieve a smooth transition between the effects of the data term and the interface term. $\tilde{I}_{iG} = 1 - I_{iG}$ is the inverse weight. With that, we formulate the overall loss L_D as

$$L_D(I_o, I_t, I_i) = L_2(I_o \odot \tilde{I}_{iG}, I_t \odot \tilde{I}_{iG}) + \lambda S_D(I_o, I_t, I_i), \quad (1)$$

$$S_D(I_o, I_t, I_i) = \frac{1}{|\Omega|} \sum_{x \in \Omega} ((I_o * g_{\text{psf}} - I_t) \odot I_{iG})^2, \quad (2)$$

where I_o is the network output, I_t the target image, λ the weighting of the interface term, \odot denotes the Hadamard product (element-wise multiplication) and g_{psf} a filter kernel of the point spread function (PSF). The notion is: In the target image, the interfaces are smoothed by the PSF by the process of imaging. Whereas in the output image the goal is to reduce the blurring, *i.e.*, increase the sharpness. Consequently, the term $I_o * g_{\text{psf}} - I_t$ penalizes deviations in I_o from sharp peaks. The PSF in this case could be the result of a per-image estimation, learned for one specific system, manually determined for one system or treated as hyper-parameter. We assumed the PSF to be an anisotropic Gaussian, with $\sigma_{\text{psf}}^x = \text{FWHM}_{\text{lat}}/2$ and $\sigma_{\text{psf}}^y = \text{FWHM}_{\text{ax}}/2$ determined experimentally from a simulated

point reflector, where we measured the full width half maximum (FWHM) in lateral and axial directions. The hyper-parameters and their values are listed in Table 4.

Parameter	Value
λ	500
learning rate	3×10^{-5}
epochs	1000
σ_i (interface)	0.375 mm $\hat{=}$ 5 pixels
σ_{psf}^y (axial)	0.075 mm $\hat{=}$ 1 pixel
σ_{psf}^x (lateral)	0.525 mm $\hat{=}$ 7 pixels

Table 4: Training hyper-parameters and their values

4. Evaluation

In order to achieve a fair comparison we evaluate our approach to a group of well-established and state-of-the-art speckle filters, and provide qualitative comparisons and quantitative evaluations for the simulated, phantom, and in-vivo datasets in the following. To this end, we compare the results of our method against SRAD¹ (Yu and Acton, 2002), median filter², bilateral filter² (Tomasi and Manduchi, 1998), non-local means² (NLM) (Buades et al., 2005), and optimized Bayesian non-local means³ (OBNLM) (Coupé et al., 2009). Table 5 contains the parametrization used for the mentioned methods.

Method	Parameter	Value
SRAD	number of iterations	200
	lambda	0.1
Median	window size	15
Bilateral	degree of smoothing	0.05
	spatial sigma	5
NLM	degree of smoothing	0.075
	search windows size	101
	comparison window size	21
OBNLM	search area size	101
	patch size	45
	degree of smoothing	1.05

Table 5: Comparison method parameters and their values after manual tuning on the image in Figure 7a.

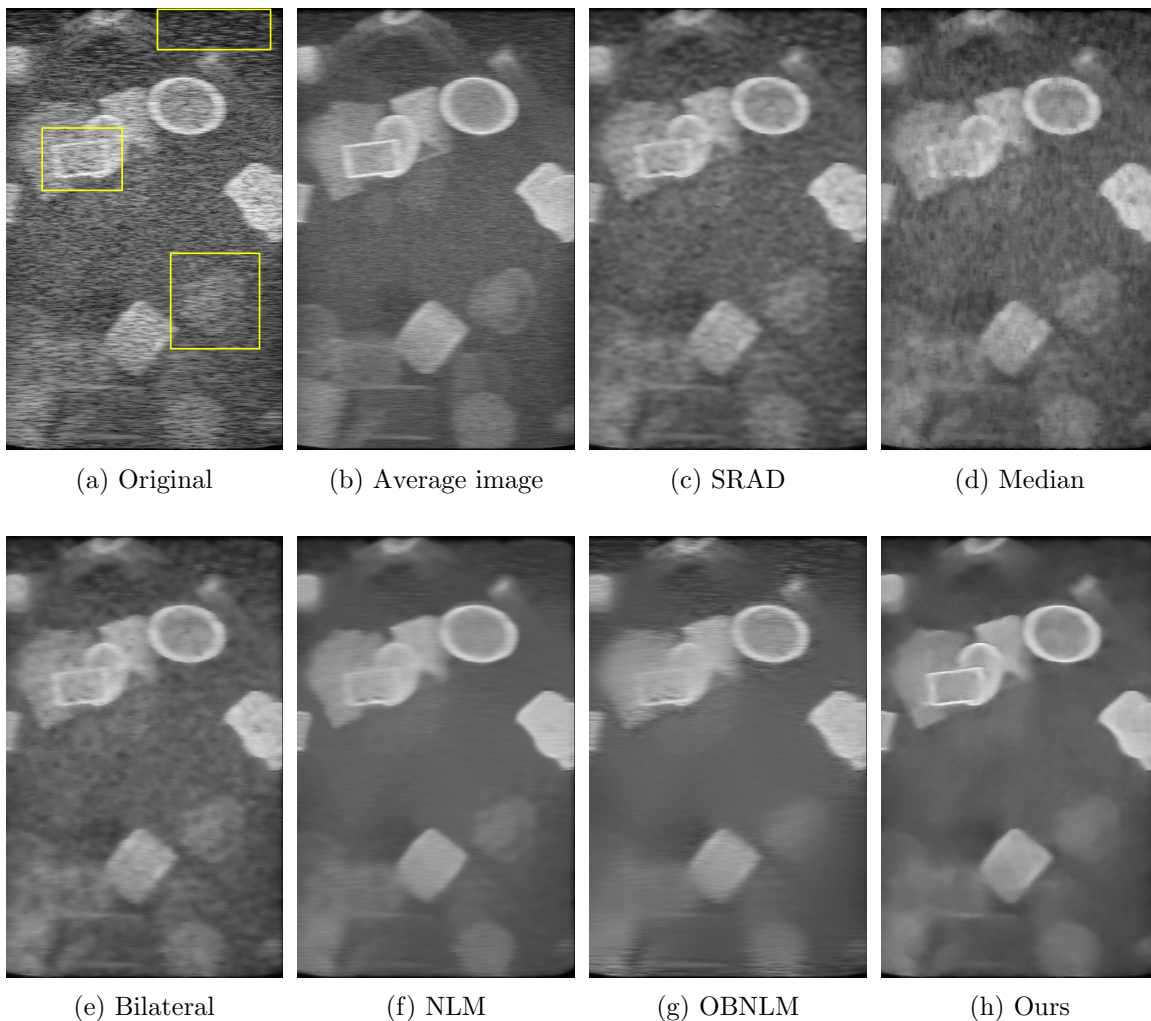


Figure 5: Qualitative comparison on a simulated image. The original speckled image (a), the average of nine different scatterer instantiations (b), output of SRAD (c), median filter (d), bilateral filtering (e), NLM (f), OBNLM (g) and ours (h).

4.1 Qualitative comparison

Simulated data. In the simulated image from the validation set (see subsection 3.2) shown in Figure 5, we can visually compare the result of applying the different methods directly with the average image of nine speckle instances. It is clear that SRAD (c), median filtering (d) and the bilateral filter (e) mostly change the appearance of the speckle, but do not

-
1. implementation from Virginia Image and Video Analysis, School of Engineering and Applied Science, University of Virginia (2006)
 2. implementation from MATLAB R2020b
 3. implementation from Coupé (2011)

fully remove it. NLM (f), OBNLM (g) and our method (h) all remove the speckle very well. In the outlined area in the top of the image, the less dense speckle is not fully removed by OBNLM. Another noteworthy region is the rectangular object in the top left that has a bright interface in the input as well as the average image. NLM and OBNLM do not retain this feature with high contrast, whereas our method shows contrast close to the average image. The elliptic object in the bottom right appears in our method not as clearly as it is visible in the average image, we believe this is due to comparatively low brightness of interface around it. The other methods, however, also struggle to highlight the object.

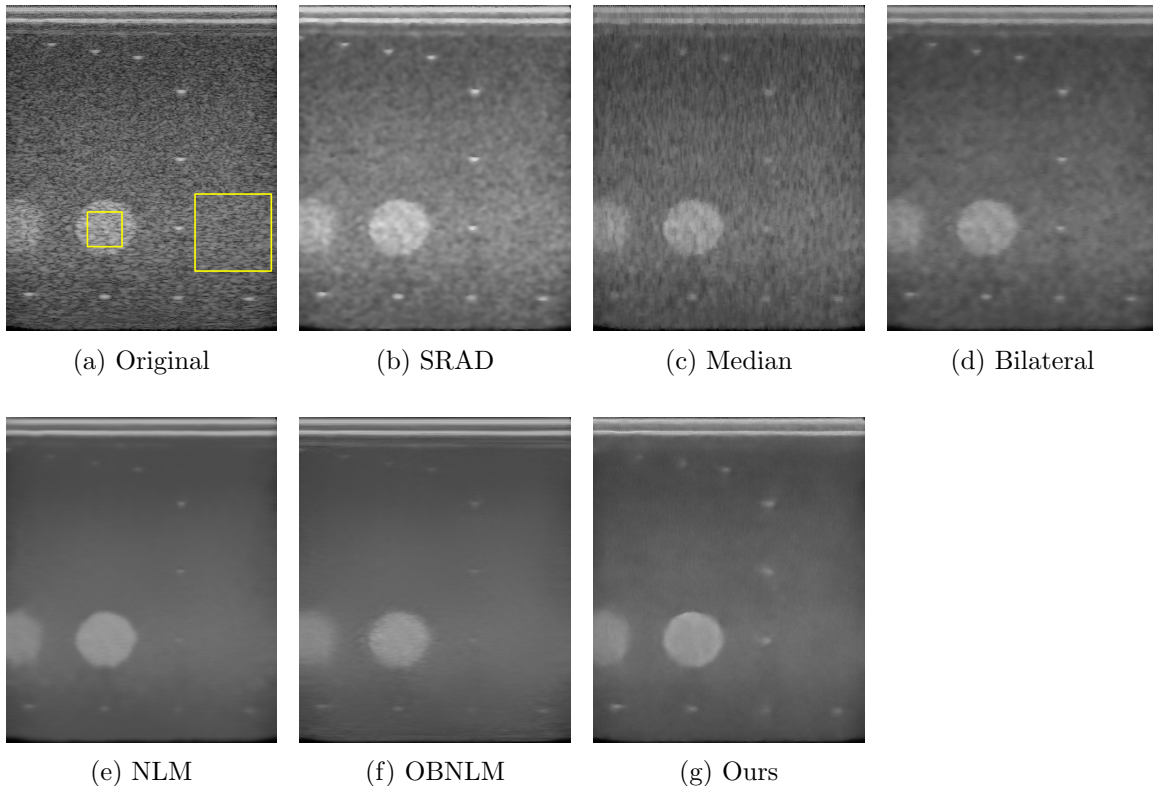


Figure 6: Qualitative comparison on an experimental phantom image. The original speckled image (a), the output of SRAD (b), median filter (c), bilateral filtering (d), NLM (e), OBNLM (f) and ours (g). The marked regions in the inclusion and background are used for quantitative evaluation.

Phantom data. The experimental image in Figure 6 shows an ultrasound quality assurance phantom (Model 040GSE, CIRS Inc., Norfolk, VA, USA). The image was acquired with a CPLA12875 probe and a cQuest Cicada (both Cephasonics, CA, USA), with equivalent imaging parameters as used for the simulations (see Table 2), but with an imaging depth of 45 mm. Being acquired from a physical phantom, there is no average image as reference, but the distinct regions in the phantom are constructed as regions of homogeneous scattering. The image shows a background region, several string reflectors, as well

as two different circular hyper-echoic inclusions. The result of SRAD (b), median (c) and bilateral (d) show the same general patterns as with the simulated data—not succeeding in completely removing the speckle. NLM (e), OBNLN (f) and our method (g) are again close to that goal. While NLM shows the smoothest image among the three methods and shows a sharp edge of the bright inclusion, it suppresses the string responses more. The result of OBNLN is almost as smooth as NLM overall, but it shows inhomogeneities around the bright inclusion and its outline is not as well defined as with the other methods. Our method—while smooth locally—shows a certain inhomogeneity in the background, but does not suppress the point reflectors as strongly and has a clear demarcation of both inclusions.

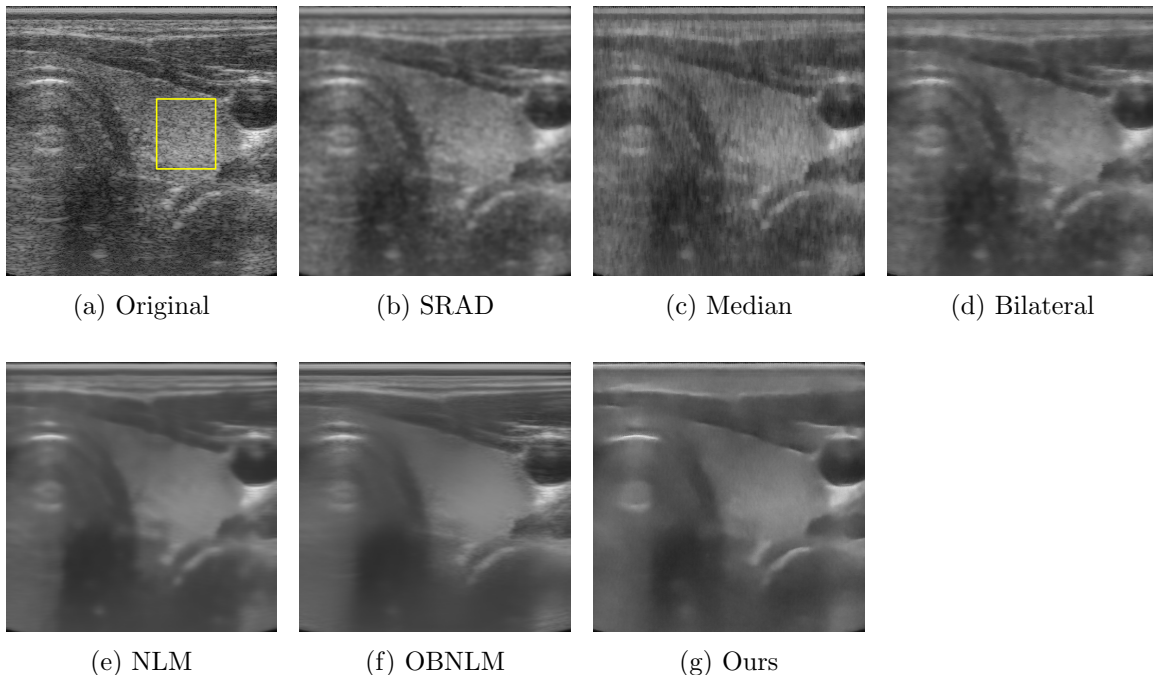


Figure 7: Qualitative comparison on an in-vivo image. The original speckled image (a), the output of SRAD (b), median filter (c), bilateral filtering (d), NLM (e), OBNLN (f) and ours (g). The marked region in the thyroid is used for quantitative evaluation.

In-vivo data. In the in-vivo image in Figure 7—a cross-sectional view of the thyroid of a healthy volunteer acquired with the same configuration as the phantom data with 35 mm depth—we can see that SRAD (b), median (c) and bilateral filtering (d) perform better than in the simulated and experimental cases, although NLM (e), OBNLN (f) and our method (g) exhibit a significantly more homogeneous appearance in the thyroid and especially OBNLN and our method retain more sharpness in comparison. While OBNLN better captures the muscle interfaces over the carotid artery on the right of the image compared to our method, it is also less smooth in the overall area of the carotid. Our method does not retain said interfaces completely, but is not disturbed by the clutter within the artery.

4.2 Quantitative evaluation

Simulated data. For the quantitative evaluation in the simulated case we utilize the average images as an approximation of the speckle-free image. We perform this for all 100 simulated images in the validation set and the corresponding average images. The input images are scaled to the range $[0, 1]$ before application of any of the methods. Table 6 shows the mean and standard deviation of the mean squared errors (MSE) and the mean absolute differences (MAD) between the considered methods and the average images. All methods

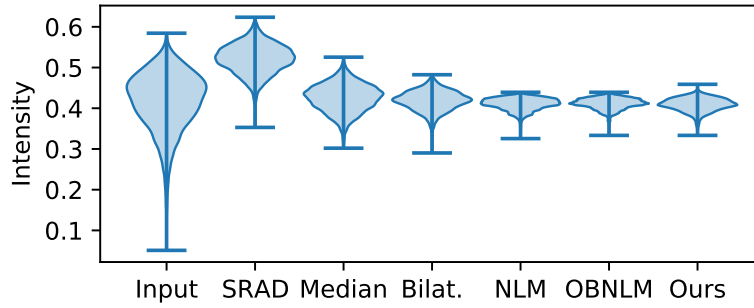
Method	MSE ($\times 10^{-3}$)	MAD ($\times 10^{-2}$)
Input	5.87 ± 1.31	5.86 ± 0.87
SRAD	2.33 ± 0.86	3.61 ± 0.76
Median	1.82 ± 0.25	3.25 ± 0.33
Bilateral	1.48 ± 0.20	2.94 ± 0.30
NLM	$1.27 \pm \mathbf{0.09}$	$2.70 \pm \mathbf{0.13}$
OBNLN	1.48 ± 0.15	2.87 ± 0.20
Ours	$\mathbf{1.20} \pm 0.11$	$\mathbf{2.60} \pm 0.20$

Table 6: Quantitative comparison on 100 simulated images from the validation set. It shows the mean and standard deviation of the MSE and the MAD between images processed with each methods (and the unprocessed input) against the average images of nine speckle instances. Lowest error mean and standard deviation for both MSE and MAD are highlighted in bold without implying significance.

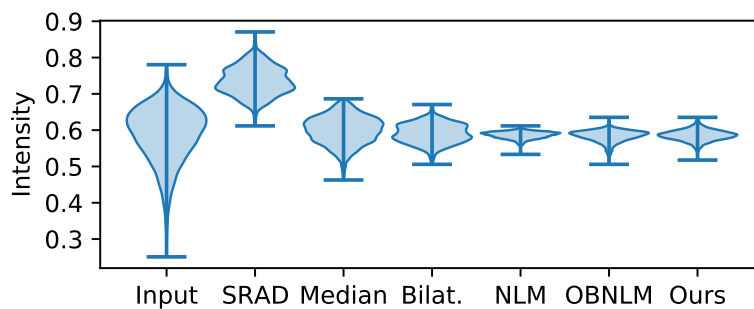
besides SRAD and median show a similar performance with respect to MSE and MAD, where our method yields the best result. In combination with the clearly varying image appearance of the different methods, this emphasizes the trade-offs between the methods compared here.

Phantom and in-vivo data. In the experimental and in-vivo images it is not possible to observe different speckle instantiations and thus no average image can be computed. Consequently, we focus on homogeneous image regions, namely the hyperechoic inclusion and the background for the phantom dataset (see Figure 6a) as well as the thyroid in the in-vivo dataset (see Figure 7a). Within those regions of assumed homogeneous scatterer distribution the ideal speckle removal filter would result in a flat response. Figure 8 shows violin plots of the intensity distribution in the marked regions of the phantom images, while Figure 9 shows those of the in-vivo image regions. The results of NLM, OBNLN and our method on the experimental image show very similar distributions; SRAD, median and bilateral-filter however are less tightly packed. This generally is matched by the evaluation for the in-vivo image data, but the distribution of our method is less pronounced than NLM and OBNLN.

In Table 7, we show the image intensity standard deviations within the homogeneous image regions. As expected from the violin plots, SRAD, median, and the bilateral-filter exhibit larger standard deviations in the three regions than NLM, OBNLN and our method. While our method does not outperform NLM and OBNLN—which share best performance within the three regions and were tuned on the thyroid image—it shows how well our method translates to real ultrasound data, despite not having been trained with real images.



(a) Background



(b) Hyperechoic Inclusion

Figure 8: Image intensity distribution within homogeneous background region (a) and hyperechoic inclusion (b) of the experimental images.

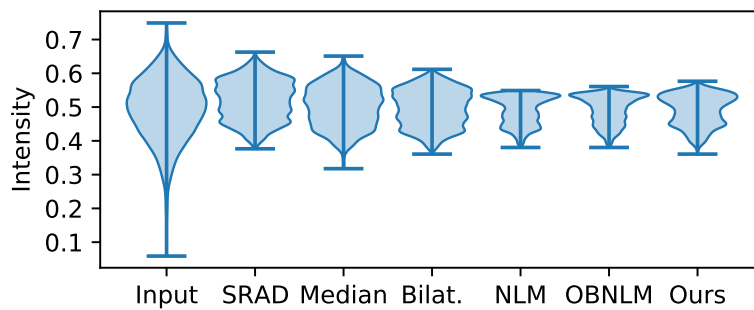


Figure 9: Image intensity distribution within homogeneous thyroid region of the in-vivo images.

5. Discussion

The qualitative and quantitative evaluations show that Speckle2Speckle works well in the simulated images, performing on-par with or even outperforming NLM and OBNLM, as can be seen in Figure 5 and Table 6. It also performs well in real acquisitions, although no real images have been used for training. There are shortcomings however, especially

Region	Experimental ($\times 10^{-2}$)		In-Vivo ($\times 10^{-2}$)
Method	Background	Inclusion	Thyroid
Input	7.10	7.58	8.96
SRAD	3.55	3.96	5.89
Median	3.37	3.83	6.05
Bilateral	2.39	2.69	5.42
NLM	1.49	0.96	4.21
OBNLM	1.32	1.60	4.20
Ours	1.61	1.51	4.54

Table 7: Quantitative evaluation on the experimental and in-vivo images and shown in Figure 6a and Figure 7a respectively. The table shows the image intensity standard deviation in homogeneous regions in the background and foreground of the experimental images, and within the thyroid in the in-vivo case. Lowest standard deviation per region highlighted in bold without implying significance.

regarding the overall smoothness as in the background area and the reproduction of the point scatterers in Figure 6. Yet, it seems the highlighting of interfaces translates well to real images, with the exception of the linear structures in the muscle layer above the carotid artery in Figure 7.

The execution time of our method is significantly lower than for NLM and OBNLM. While the used NLM and OBNLM implementations (CPU only) take in the range of minutes to execute, our method can be performed within tens of milliseconds on a recent GPU, making it suitable for real-time use.

6. Conclusion

We have shown with Speckle2Speckle a technique for training despeckling filters purely on simulated data as well as the generation of the simulated data. The concept is intriguing, since it allows for the generation of multiple speckle realizations from the same underlying geometry. The learned filter translates well to real acquisitions, performing similar to NLM and OBNLM, but only requiring a fraction of the execution time.

Since no clean training data is required, the number of simulations is drastically reduced compared to approaches that would use average images were used as target images. It also enables creation of matching maps with high-level info on the structures present in the image that can be used to guide the outcome of the method during training—as we have done with interfaces in this case.

Including single point scatterers and/or strings in the simulated images could improve the reproduction of those structures. They could be included in the interface map used for sharpening or placed in a separate map all-together, only depending on the desired appearance. This aspect of using additional geometric maps to tune the result for particular locations could possibly be exploited beyond speckle removal, for example for clutter filtering in blood vessels within the same filter pass.

Acknowledgments

We acknowledge the important conversations with our colleagues Maximilian Baust, Maria Tirindelli, and Stefan Würz.

Ethical Standards

The work follows appropriate ethical standards in conducting research and writing the manuscript, following all applicable laws and regulations regarding treatment of animals or human subjects.

Conflicts of Interest

We declare we do not have conflicts of interest.

References

- Antoni Buades, Bartomeu Coll, and J-M Morel. A non-local algorithm for image denoising. In *2005 IEEE Computer Society Conference on Computer Vision and Pattern Recognition (CVPR'05)*, volume 2, pages 60–65. IEEE, 2005.
- Simone Cammarasana, Paolo Nicolardi, and Giuseppe Patanè. A universal deep learning framework for real-time denoising of ultrasound images. *arXiv preprint arXiv:2101.09122*, 2021.
- Pierrick Coupé. Optimized bayesian non-local means filter, matlab package. <https://web.archive.org/web/20201015011836/https://sites.google.com/site/pierrickcoupe/software/denoising-for-medical-imaging/speckle-reduction/obnlm-package>, 2011. [Online; accessed 7-December-2021].
- Pierrick Coupé, Pierre Hellier, Charles Kervrann, and Christian Barillot. Nonlocal means-based speckle filtering for ultrasound images. *IEEE Transactions on Image Processing*, 18(10):2221–2229, 2009.
- Rüdiger Göbl, Nassir Navab, and Christoph Hennersperger. Supra: open-source software-defined ultrasound processing for real-time applications. *International Journal of Computer Assisted Radiology and Surgery*, Mar 2018. ISSN 1861-6429. doi: 10.1007/s11548-018-1750-6.
- Jørgen Arendt Jensen. Field: A program for simulating ultrasound systems. In *Proc. of the 6th Nordic Conf. on Human-Computer Interaction, Medical & Biological Engineering & Computing*, pages 351–353. Springer, 1996.
- Jørgen Arendt Jensen and Niels Bruun Svendsen. Calculation of pressure fields from arbitrarily shaped, apodized, and excited ultrasound transducers. *IEEE Transactions on Ultrasonics, Ferroelectrics, and Frequency Control*, 39(2):262–267, 1992.

- Alexander Krull, Tim-Oliver Buchholz, and Florian Jug. Noise2void-learning denoising from single noisy images. In *Proceedings of the IEEE/CVF Conference on Computer Vision and Pattern Recognition*, pages 2129–2137, 2019.
- Jaakko Lehtinen, Jacob Munkberg, Jon Hasselgren, Samuli Laine, Tero Karras, Miika Aittala, and Timo Aila. Noise2Noise: Learning image restoration without clean data. In Jennifer Dy and Andreas Krause, editors, *Proceedings of the 35th International Conference on Machine Learning*, volume 80 of *Proceedings of Machine Learning Research*, pages 2965–2974, Stockholmsmässan, Stockholm Sweden, 10–15 Jul 2018. PMLR.
- Sameera V. Mohd Sagheer and Sudhish N. George. A review on medical image denoising algorithms. *Biomedical Signal Processing and Control*, 61:102036, 2020. ISSN 1746-8094. doi: <https://doi.org/10.1016/j.bspc.2020.102036>.
- Olaf Ronneberger, Philipp Fischer, and Thomas Brox. U-net: Convolutional networks for biomedical image segmentation. In *International Conference on Medical Image Computing and Computer-Assisted Intervention (MICCAI’15)*, pages 234–241. Springer, 2015.
- Carlo Tomasi and Roberto Manduchi. Bilateral filtering for gray and color images. In *Sixth International Conference on Computer Vision (IEEE Cat. No. 98CH36271)*, pages 839–846. IEEE, 1998.
- Virginia Image and Video Analysis, School of Engineering and Applied Science, University of Virginia. MATLAB and C implementation of speckle reducing anisotropic diffusion (SRAD). <https://web.archive.org/web/20171213062541/http://viva-lab.ece.virginia.edu/downloads.html>, 2006. [Online; accessed 7-December-2021].
- Da Yin, Zhongzheng Gu, Yanran Zhang, Fengyan Gu, Shouping Nie, Shaotong Feng, Jun Ma, and Caojin Yuan. Speckle noise reduction in coherent imaging based on deep learning without clean data. *Optics and Lasers in Engineering*, 133:106151, 2020.
- Yongjian Yu and Scott T Acton. Speckle reducing anisotropic diffusion. *IEEE Transactions on image processing*, 11(11):1260–1270, 2002.